DOI: 10.1002/adfm.200500662

Nanostructured Vanadium Oxide Electrodes for Enhanced Lithium-Ion Intercalation**

By *Ying Wang*, *Katsunori Takahashi*, *Kyoungho Lee*, and *Guozhong Cao**

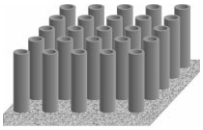

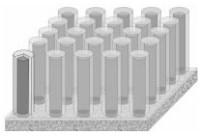

This article summarizes our most recent studies on improved Li^+-intercalation properties in vanadium oxides by engineering the nanostructure and interlayer structure. The intercalation capacity and rate are enhanced by almost two orders of magnitude with appropriately fabricated nanostructures. Processing methods for single-crystal V_2O_5 nanorod arrays, $V_2O_5{\cdot}n\,H_2O$ nanotube arrays, and Ni/$V_2O_5{\cdot}n\,H_2O$ core/shell nanocable arrays are presented; the morphologies, structures, and growth mechanisms of these nanostructures are discussed. Electrochemical analysis demonstrates that the intercalation properties of all three types of nanostructure exhibit significantly enhanced storage capacity and rate performance compared to the film electrode of vanadium pentoxide. Addition of TiO_2 to orthorhombic V_2O_5 is found to affect the crystallinity, microstructure, and possible interaction force between adjacent layers in V_2O_5, and subsequently leads to enhanced Li^+-intercalation properties in V_2O_5. The amount of water intercalated in V_2O_5 is found to have a significant influence on the interlayer spacing and electrochemical performance of $V_2O_5{\cdot}n\,H_2O$. A systematic electrochemical study has demonstrated that the $V_2O_5{\cdot}0.3\,H_2O$ film has the optimal water content and exhibits the best Li^+-intercalation performance.

1. Introduction

Intercalation-electrode materials are electroactive and serve as host solids into which guest species are reversibly intercalated from an electrolyte. Currently there are three intercalation materials that are used commercially as positive-electrode materials in lithium-ion rechargeable batteries: $LiCoO_2$, $LiNiO_2$, and $LiMn_2O_4$. $LiCoO_2$ is the most popular among the possible cathode materials because of the convenience and simplicity of its preparation. This material can be easily synthesized using both solid-state and chemical approaches.[1,2] The Li_xCoO_2 system has been studied extensively thus far;[3,4] Li_xCoO_2 exhibits excellent cyclability at room temperature for $1 > x > 0.5$. The specific capacity of the material is limited to the range 137–140 mA h g^{-1}, although the theoretical capacity of $LiCoO_2$ is 273 mA h g^{-1}.[5] Even though Li_xCoO_2 has good electrochemical properties and is easy to synthesize, it is very expensive and highly toxic. The reversible capacity of Li_xNiO_2 is higher than that of Li_xCoO_2, since the amount of lithium that can be extracted/intercalated during redox cycles is around 0.55 in comparison to 0.5 for $LiCoO_2$, allowing the specific capacity to be more than 150 mA h g^{-1} with appropriate cyclability.[6]

Although $LiNiO_2$ and $LiCoO_2$ are isostructural, the preparation of $LiNiO_2$ is more complicated. Since there are additional nickel ions on the lithium sites, and vice versa in the crystal structure of $LiNiO_2$, the Li–Ni–O system is represented by $Li_{1-y}Ni_{1+y}O_2$, a deviation from the normal stoichiometry.[7,8] This special structure makes it very difficult to synthesize the stoichiometric oxide with all the lithium sites completely filled by lithium.

[*] Dr. G. Z. Cao, Y. Wang
Materials Science and Engineering Department
University of Washington
Box 352120, Seattle, WA 98195-2120 (USA)
E-mail: gzcao@u.washington.edu
Dr. K. Takahashi
Steel Research Laboratory, JFE Steel Corporation
Chuo-ku, Chiba 260-0835 (Japan)
Dr. K. H. Lee
Materials Engineering Department, Soonchunhyang University
646 Eupnae-Ri, Shinchang-Myun, Asan-Si, Chungnam-Gun (Korea)

[**] This work has been supported in part by the National Science Foundation (DMI-0455994). This work has also been supported by the Center for Nanotechnology at UW, Pacific Northwest National Laboratories (PNNL), Joint Institute of Nanoscience and Nanotechnology (JIN, UW and PNNL), Washington Technology Center (WTC), and JFE Steel Corporation, Japan. Wang's work was supported by Ford, Nanotechnology, and JIN graduate fellowships, JFE Steel Corporation supportedTakahashi's research, and Lee's work was supported by Soonchunhyang University, S. Korea. A portion of the research (TEM study) described in this paper was performed in the Environmental Molecular Sciences Laboratory, a national scientific user facility sponsored by the Department of Energy's Office of Biological and Environmental Research and located at PNNL.

$LiMn_2O_4$ is the third most popular cathode material for lithium-ion batteries. In comparison with $LiCoO_2$ and $LiNiO_2$, $LiMn_2O_4$ is less toxic and has an abundant source. In principle, $Li_xMn_2O_4$ permits the intercalation/extraction of lithium ions in the range $0 < x < 2$.[9] For values of x between 1 and 2 the material consists of two different phases—cubic in the bulk and tetragonal at the surface. Simultaneously, the intercalation of lithium ions effectively decreases the average valence of manganese ions and leads to a pronounced cooperative Jahn–Teller effect, in which the cubic spinel crystal becomes distorted tetragonal with $c/a \approx 1.16$, and the volume of the unit cell increases by 6.5 %. This high c/a ratio causes a low capacity restricted to ~120–125 mA h g^{-1} and significant capacity degradation at moderate temperatures in the range 50–70 °C.[10]

The limitations of the commercial cathode materials have stimulated a lot of research activity targeted at investigating cathode materials for lithium-ion batteries. The reader is referred to excellent reviews on Li-ion intercalation materials for lithium secondary batteries, such as the review articles by Winter and co-workers,[11,12] Aricò et al.,[13] and the recent book chapter by Maranchi et al.[14] V_2O_5 offers the advantages of being cheap, easy to synthesize, and having high energy densities and, thus, has attracted much interest.[11] V_2O_5 consists of layers of VO_5 square pyramids that share edges and corners.[9,15] The apical V–O bond corresponds to a double bond that is much shorter than the other four bonds. Aside from this two-dimensional character, the structure of V_2O_5 can also be described as being distorted VO_6 octahedral.[16,17] The very long sixth V–O bond underlines the structural anisotropy of this material and the ability to insert guest species in perovskite-like cavities. Electrochemical lithium-ion intercalation occurs together with compensating electron intercalation, leading to the formation of vanadium bronzes as follows:

$$V_2O_5 + x\,Li^+ + x\,e^- \rightarrow Li_xV_2O_5 \quad (1)$$

In addition to crystalline V_2O_5, rather promising results have been reported for hydrated vanadium pentoxide ($V_2O_5{\cdot}n\,H_2O$), such as $V_2O_5{\cdot}n\,H_2O$ glasses with P_2O_5 or other network formers,[18] $V_2O_5{\cdot}n\,H_2O$ xerogels,[19,20] and $V_2O_5{\cdot}n\,H_2O$ aerogels.[21] These amorphous or low-crystalline materials offer considerable advantages by virtue of their morphology. A large electrochemically active surface area, small particle size, and low density provide both high overall diffusion coefficients and low volume expansion during lithium intercalation. Specific energies of over 700 W h kg^{-1} were measured for lithium cells with xerogel cathodes.[20] $V_2O_5{\cdot}n\,H_2O$ xerogels are composed of ribbonlike particles and display lamellar ordering, with water molecules intercalated between the layers.[22] These water molecules expand the distance between the layers and, as a result, the intercalation capacities of $V_2O_5{\cdot}n\,H_2O$ xerogels are enhanced.[20] However, the intercalation capacity and charge/discharge rate of V_2O_5 are limited by the moderate electrical conductivity (10^{-2}–10^{-3} S cm^{-1})[23,24] of V_2O_5 and the low diffusion coefficient of Li ions (10^{-12}–10^{-13} $cm^2\,s^{-1}$)[25,26] in the V_2O_5 matrix. Many studies have been conducted to improve lithium diffusion and electrical conduction performance in V_2O_5 by crystal-structure modification to-

Guozhong Cao is an Associate Professor of Materials Science and Engineering and Mechanical Engineering at the University of Washington. He received his Ph.D. degree from Eindhoven University of Technology (the Netherlands) in 1991. Before joining the UW faculty in 1996, Dr. Cao worked briefly at the University of Twente, Univerity of Nijmegen, and Advanced Materials Laboratory (University of New Mexico and Sandia National Laboratory). His major awards include the European Union Fellowship in 1993, the college Outstanding Educator Award in 1999, and the university Distinguished Teaching Award in 2000. He has published over 180 refereed papers on a wide range of materials science topics, edited three conference proceedings, and authored a book, "Nanostructures and Nanomaterials: Synthesis, Properties and Applications" in 2004.

Ying Wang was born in Jiangsu, China, in 1977. She received a B.S. degree in Chemical Physics from the University of Science and Technology of China in 1997 and an M.S. degree in Chemistry from Harvard University in 1999. She is now a Ph.D. candidate under the supervision of Professor Guozhong Cao in the Department of Materials Science and Engineering at the University of Washington. Her research interests include sol–gel processing, electrochemical and eletrophoretic deposition, nanostructured materials, intercalation materials for energy storage/conversion, electrochromic displays, batteries, and supercapacitors. Her recent awards include the Nanotechnology Graduate Research Award from the University of Washington Initiative Fund (UIF, 2005), a Graduate Fellowship from the PNNL-UW Joint Institute for Nanoscience (JIN, 2005), and a Ford Motor Company Fellowship (2004). She has published over 15 journal papers and authored three book chapters.

ADVANCED FUNCTIONAL MATERIALS

wards a more open structure[27] and by coating V_2O_5 on highly conductive materials.[28] Other approaches include making use of nanostructured materials that possess large surface areas and short diffusion paths.

Ordered arrays of nanorods, nanotubes, or core/shell nanocables are some of the most promising nanostructures for Li^+-intercalation applications. Patrissi and Martin investigated the electrochemical properties of V_2O_5 nanorod arrays made by depositing vanadium pentoxide sols within the pores of polycarbonate (PC) membranes, and reported that nanorod arrays achieved four times the capacity of a thin-film electrode at high discharge rate.[29] Compared to nanorods, nanotubes possess several different areas of contact, i.e., the inner and outer wall surfaces, as well as the open ends. In principle, nanotube arrays have even larger surface areas than nanorod arrays. In addition, the tubes can operate as electrolyte-filled channels for faster transport of the ions to the intercalation sites. Mixed-valent vanadium(+4, +5) oxide nanotubes (VO_x-NTs) have been obtained in high yield by treating a vanadium(v) oxide precursor with an amine that has long alkyl chains, followed by hydrolyzation and hydrothermal reaction.[30] The amine functions as a molecular structure-directing template, and the resulting VO_x-NT has a scroll-like morphology. This material opens new perspectives for Li^+-intercalation applications and has been widely studied recently. Several research groups have measured discharge capacities up to 200 mA h g^{-1},[31,32] though its morphological flexibility leads to rapid degradation of capacity.[33]

Another approach to increase the intercalation capacity of V_2O_5 is to modify its interlayer structure and the interaction forces between the adjacent layers. When the distance between adjacent V_2O_5 layers increases, the insertion capacity increases. For example, $V_2O_5{\cdot}n\,H_2O$ possesses a Li^+-intercalation capacity that is about 1.4 times larger than that of V_2O_5.[34] The distance between the adjacent layers in $V_2O_5{\cdot}n\,H_2O$ is 11.52 Å,[35] compared to an interlayer distance of 4.56 Å in orthorhombic V_2O_5. It has been found that $V_2O_5{\cdot}n\,H_2O$ exhibits an even larger capacity and good cycling performance when the water content in $V_2O_5{\cdot}n\,H_2O$ is reduced by thermal treatment, and the influence of heat treatment on $V_2O_5{\cdot}n\,H_2O$ has been studied using $V_2O_5{\cdot}n\,H_2O$ synthesized from $NaVO_3$.[36–39] Doping or substitution in V_2O_5 by other cations with different valance states have been used to tailor the interaction forces between two adjacent layers in the intercalation compound. Several materials, such as Ni,[40] Ce,[41] Ag, and Cu,[42] have been reported to enhance the capacity of V_2O_5 by forming bronze structures with it. Titanium has the valence state +4 in TiO_2 and the diameter of titanium is similar to that of vanadium with a coordination number of 6. However, there has been some debate in the literature as to the impact of doping with TiO_2. For example, Minett and Owen[43] showed improved cyclic reversibility of mixed vanadium oxide/titanium oxide systems over that of V_2O_5. However, their mixed-oxide system possessed a lower capacity than V_2O_5. Davies et al. found that the improved cycling stability of the V_2O_5/TiO_2 system might be caused by a preferential reduction of Ti^{4+} to Ti^{3+}, which prevents a reorganization of the microstructure in the material.[44] Özer et al. found that addition of 5 mol % TiO_2 to V_2O_5 greatly improved the intercalation capacity.[45] It is clear that, although it is agreed on in the literature that the cycling stability of the mixed V_2O_5/TiO_2 system is improved, there are different findings on the Li^+-intercalation properties of V_2O_5 on addition of TiO_2.

In this paper, we summarize our recent studies on various nanostructures of orthorhombic V_2O_5 and low-crystalline $V_2O_5{\cdot}n\,H_2O$, including single-crystal V_2O_5 nanorod arrays,[34,46,47] $V_2O_5{\cdot}n\,H_2O$ nanotube arrays,[48] and Ni/$V_2O_5{\cdot}n\,H_2O$ core/shell nanocable arrays.[49] The fabrication of such nanostructures has been accomplished using template-based growth by sol electrophoretic deposition[50–55] and electrochemical deposition.[56] Figure 1 shows schematics of arrays of V_2O_5 nanorods, $V_2O_5{\cdot}n\,H_2O$ nanotubes, and Ni/$V_2O_5{\cdot}n\,H_2O$ core/shell nanocables. In addition, platelet- and fibrillar-nanostructured V_2O_5 films have been prepared by solution methods, and their electrochemical Li^+-intercalation properties have been studied in our laboratory.[57] These platelet and fibrillar films consist of randomly oriented nanoscale V_2O_5 particles and fibers, respectively, protruding from the substrate surface. These nanostructured films exhibit relatively larger surface areas and shorter diffusion paths for Li^+ intercalation than the plain thin-film structure. The processing methods, discharge capacities, and cyclic performance of these films are compared with those of the conventional plain film. We have recently investigated the thermal behavior and the electrochemical performance of $V_2O_5{\cdot}n\,H_2O$ films synthesized using the H_2O_2–V_2O_5 route, together with the effect of water content on the interlayer spacing and electrochemical performance.[58] Furthermore, we have found that the electrochemical intercalation properties of V_2O_5 are significantly enhanced on addition of TiO_2.[59] Films and nanorod arrays of V_2O_5/TiO_2 composites have been fabricated in our laboratory to investigate the effect

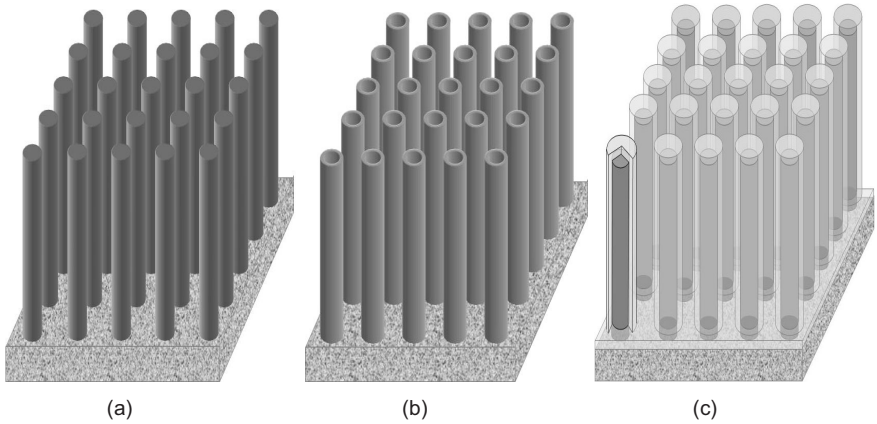

Figure 1. Schematics of vanadium pentoxide a) nanorod, b) nanotube, and c) nanocable arrays.

of TiO_2 addition.[59,60] All the electrochemical characterizations were carried out in a standard three-electrode cell, with a Pt mesh serving as the counter electrode, Ag/Ag^+ as the reference electrode, and 1 M $LiClO_4$/propylene-carbonate as the electrolyte. In the following sections, experimental information including sample preparation will be discussed; for details of the experiments, the reader is referred to our previous publications.

2. Engineering of Vanadium Oxide Nanostructures

Single-crystal V_2O_5 nanorod arrays have been grown by electrochemical deposition, surface condensation induced by a change of local pH as a result of H_2O electrolysis, and sol–gel electrophoretic deposition, combined with template growth methods.[46] Single-crystal V_2O_5 nanorod-array electrodes deliver a capacity that is five times higher than that of sol–gel-derived films at a current density of 0.7 $A\,g^{-1}$.[34] A similar template-based electrodeposition from $VOSO_4$ solution has been employed to grow nanotube arrays of $V_2O_5{\cdot}n\,H_2O$, by using a lower voltage and shorter deposition time than those use in preparing the nanorod arrays.[48] The nanotubes have a length of 10 μm, an outer diameter of 200 nm, and an inner diameter of 100 nm. The nanotube array delivers a high initial capacity of 300 $mA\,h\,g^{-1}$, which is about twice that of the electrochemically deposited V_2O_5 film. Although the nanotube array shows more drastic degradation than the film under redox cycling, it reaches a stabilized capacity of 160 $mA\,h\,g^{-1}$, which is 1.3 times the stabilized capacity of the film. Furthermore, a two-step electrodeposition method has been used to prepare Ni/$V_2O_5{\cdot}n\,H_2O$ core/shell nanocable arrays.[49] Both the specific energy and specific power of such nanocable arrays are higher than those of the V_2O_5 film electrode by at least one order of magnitude. Such significant improvement in electrochemical performance is due to the large surface area, short diffusion distance, and reduced internal resistance offered by the nanostructure. Ni/$V_2O_5{\cdot}n\,H_2O$ nanocable arrays have also been prepared and it has been demonstrated that, at a current density of 1.6 $A\,g^{-1}$, the Li^+-intercalation capacity of the Ni/$V_2O_5{\cdot}n\,H_2O$ nanocable array is approximately 10 times higher than that of the single-crystal V_2O_5 nanorod array, and 20 times higher than that of the sol–gel-derived V_2O_5 film. These results confirm that the specific surface area of the electrode is important since the redox or intercalation reactions occur at and near the electrode interface with electrolyte; hence, nanostructured electrodes are effective for use in Li^+-ion intercalation processes.

2.1. Single-Crystal V_2O_5 Nanorod Arrays

Vanadium pentoxide nanorod arrays have been grown inside 200 nm diameter PC templates with the assistance of an electric field in three different media, i.e., a VO^{2+} solution (route A), a VO_2^+ solution (route B), and a V_2O_5 sol (route C). The pure orthorhombic phase of V_2O_5 was obtained by sintering the nanorod arrays at 485 °C in air for one hour, and the PC membrane was pyrolyzed as a result. It is worth noting that, under otherwise comparable growth conditions, the nanorods grown by electrochemical deposition showed negligible shrinkage, whereas those grown via a pH change showed a noticeable 15 % lateral shrinkage; moreover, the nanorods grown from sol electrophoretic deposition showed a substantial lateral shrinkage of 50 %. Such significant differences in lateral shrinkage of the three nanorods upon firing can be explained by their distinctively different growth mechanisms.

Figure 2 shows scanning electron microscopy (SEM) and transmission electron microscopy (TEM) images of V_2O_5 nanorod arrays grown from a VO^{2+} solution by electrochemical deposition (route A). The images show that the nanorods are arranged almost parallel to one another; the distortion is ascribed to the deformation of the PC membrane during pyrolysis. There is negligible shrinkage along the long axis, but the morphologies and diameters of nanorods grown from different solutions or sols are different. Nanorods grown from solution (routes A and B) have a uniform diameter throughout their entire length with a smooth surface. Nanorods grown by route C, however, have narrower diameters and slightly rough surfaces. X-ray diffraction (XRD) patterns (not shown here) reveal that

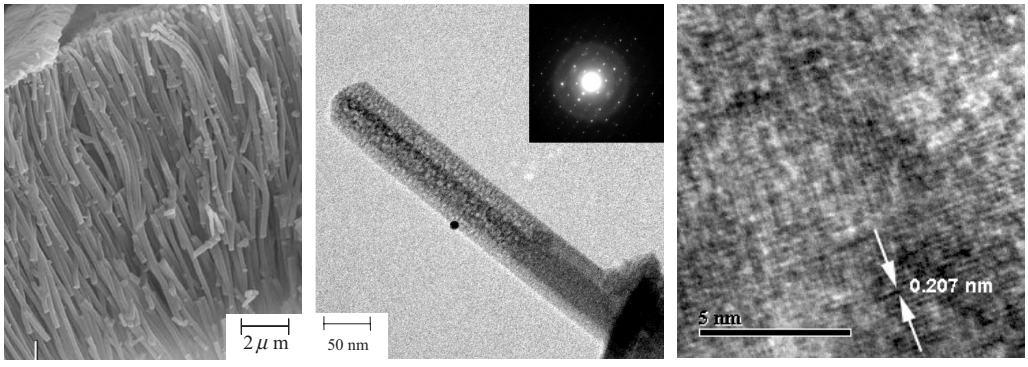

Figure 2. SEM image of a V_2O_5 nanorod array (left). High-resolution TEM images (center and right) and electron diffraction pattern (inset in center) of a V_2O_5 nanorod. The nanorods were fabricated by using the template-based electrochemical deposition from a $VOSO_4$ solution. Adapted with permission from [34]; copyright 2004, American Chemical Society.

ADVANCED FUNCTIONAL MATERIALS

all the nanorod arrays have the same V_2O_5 crystal structure after firing at 485 °C regardless of the growth method and initial solution used. Although Figure 2 presents a typical TEM image and a selected-area electron diffraction pattern of V_2O_5 nanorods grown by electrochemical deposition (route A), no appreciable difference among the nanorods grown by the three different methods was observed, as shown in our recent publication.[46] The TEM image and selected area electron diffraction pattern of a single V_2O_5 nanorod clearly demonstrate the single-crystalline, or, at least well-textured, nature of the grown nanorods, with a [010] growth direction for nanorods grown from both routes. The spacing of the fringes was measured to be 0.207 nm for the nanorods grown by route A, (and 0.208 nm for the nanorods made by route C). These values are similar for the different synthesis routes and correspond well with the spacing of (202) planes of 0.204 nm. These fringes make an angle of 88.9° with the long axes of the nanorods, which is consistent with a [010] growth direction. Similar measurements made on high-resolution images of other nanorods also yield results consistent with a [010] growth direction. Nanorods with the same orientation are grown from both solutions and the sol, but the formation mechanisms of the single crystal are different. The formation of single-crystal nanorods from solution, by both electrochemical deposition (route A) and pH-change-induced surface condensation (route B), is attributed to evolution selection growth. The initial heterogeneous nucleation or deposition on the substrate surface results in the formation of nuclei with random orientation. The subsequent growth of various facets of a nucleus is dependent on the surface energy and varies significantly from one facet to another.[61] In the case of nanorods made from a sol by electrophoretic deposition (route C), the formation of single-crystal nanorods is explained by so-called homoepitaxial aggregation of crystalline nanoparticles. It is thermodynamically favorable for the crystalline nanoparticles to aggregate epitaxially; such growth behavior and such a mechanism have been well reported in the literature.[62,63]

The cyclic voltammograms (CVs) of V_2O_5 nanorod arrays and the sol–gel film were measured using a scan rate of 1 mV s^{-1} (not shown here). The CVs of the nanorod arrays grown from route A show cathodic peaks at –0.3 and –1.1 V, which correspond to Li^+ intercalation, and one anodic oxidation peak at 0 V and one broad anodic peak at –0.7 V, which are attributed to Li^+ extraction. Masetti and co-workers[40] have also reported similar CVs that have a combination of one obvious anodic peak and two cathodic peaks. For sol–gel films, in addition to the anodic peak at 0 V, another anodic peak at –0.7 V is apparently observed; furthermore, the cathodic peaks at –0.3 and –1.1 V are less distinct. The integrated areas of the CV curves of nanorod arrays and sol–gel films are similar, which implies that both the nanorod arrays and the films possess the same specific energy at this scan rate. However, the extraction and intercalation kinetics are different, as evidenced by the sharp peaks obtained from the nanostructures produced by the solution route, compared to the far-less-distinctive peaks in the CV of the sol–gel film. The behavior of the CV of the nanorod array made from the sol (route C) is intermediate with those of the nanorod arrays grown from solution (routes A and B) and the sol–gel film, although the nanorods made from all three routes are single crystalline.

Figure 3 shows the comparison between the current density and Li^+-intercalation capacity of nanorod arrays and sol–gel films measured by chronopotentiometry. In general, for a given Li^+-intercalation capacity, e.g., for $Li_{0.7}V_2O_5$, nanorod arrays made from the solution route possess a current density that is up to five times larger than that of the sol–gel films, and larger than that of the sol electrophoresis nanorod. Similarly, for a

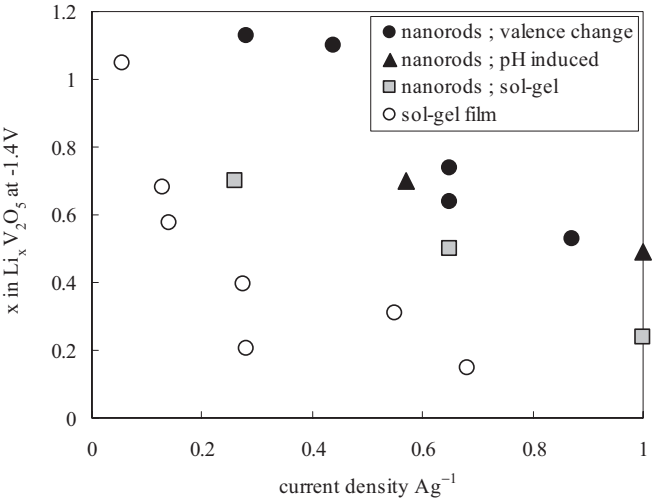

Figure 3. Plot of discharge capacity versus current density for both V_2O_5 nanorod arrays and sol–gel-derived films. Reproduced with permission from [46]; copyright 2005, The Japan Society of Applied Physics.

given current density, such as 0.7 A g^{-1}, nanorod arrays can store up to five times more Li than sol–gel films and more Li than the sol-electrophoresis nanorods. The differences in electrochemical properties observed in vanadium pentoxide nanorod arrays and films are attributed to the differences in microstructure and nanostructure. V_2O_5 nanorods grown by electrochemical deposition from solution (routes A and B) are dense single crystals, with layers parallel to the nanorod axes. Such structure is extremely favorable to Li^+ intercalation and extraction, since the surface oxidation and reduction reactions occur along the surfaces of nanorods and the solid-state diffusion distance is very small, ca. 100 nm, half of the diameter of the nanorods. In addition, such a structure permits the most freedom for dimensional change that accompanies intercalation and extraction reactions. Such well-aligned structures will also enhance the Li^+ diffusion through the solvent. Nanorods grown via sol electrophoresis (route C) are also single crystalline and well aligned, but have many defects inside the crystal; this may cause the differences among these nanorod array electrodes. Sol–gel-derived V_2O_5 films are polycrystalline and consist of platelet V_2O_5 grains with the [001] direction being perpendicular to the substrate surface. Therefore, the Li^+-intercalation and -extraction processes will comprise of Li^+ diffusion through grain boundaries, oxidation and reduction reactions at the surfaces of individual crystal grains, and diffusion inside in-

dividual grains. Thus, the difference in microstructure will have similar effects on the kinetics of charge transport.

V_2O_5 is also an electrochromic material that exhibits a reversible optical change from a transparent to a colored state upon extraction and intercalation of lithium ions.[64] Figure 4 shows the change in transmittance intensity at 700 nm as a function of time when an external voltage of 3.0 V is applied to the V_2O_5 nanorod array grown by electrophoretic deposition from a sol and the sol–gel-derived V_2O_5 film. A 30 % reduction was achieved in ca. 50 s for the V_2O_5 nanorod array; however, a time of 300 s was required for the film. The transmittance change in the nanorod array reached saturation in 3 min, while the sol–gel-derived film was not yet saturated after 5 min. Extrapolation of the data in Figure 4 suggests that the sol–gel film will require at least ten minutes to reach the same saturation, i.e., the sol–gel film has a response speed that is three times slower than that of the nanorod array. In conclusion, both the extent and speed of change in transmittance intensity of the nanorod array are significantly faster than those of the sol–gel-derived film, corroborating an enhanced electrochemical intercalation process in nanorod arrays caused by a large surface area for surface redox reactions, and short and easy diffusion paths for mass and charge transport.

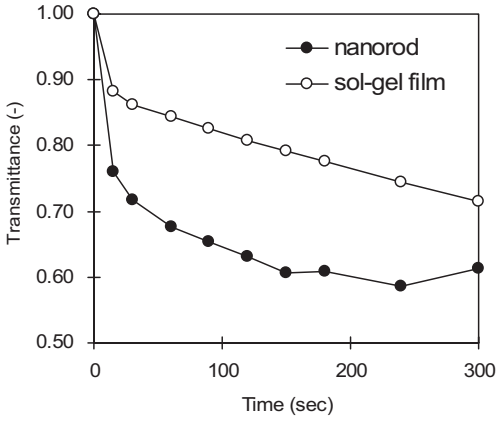

Figure 4. Transmittance intensity of nanorod arrays and sol–gel films subjected to an externally applied electric field as a function of time. Reproduced with permission from [47]; copyright 2005, American Institute of Physics.

2.2. $V_2O_5 \cdot n\,H_2O$ Nanotube Arrays

Nanotube arrays of $V_2O_5 \cdot n\,H_2O$ were grown from a VO^{2+} solution using a similar template-based electrodeposition method. The deposition voltage is lower and the deposition time shorter compared to those used for nanorod growth.[48] The applied electric voltage ranged from 1.5 to 2 V, and the deposition lasted up to 2 h. Upon completion of deposition, the sample was dried at 110 °C for 6 h and was then attached to an indium tin oxide (ITO) substrate with silver paste (Ted Pella Inc.). The as-prepared sample on the ITO substrate was dried at 110 °C for another 6 h and was immersed in methylene chloride to dissolve the PC membrane, resulting in an ensemble of $V_2O_5 \cdot n\,H_2O$ nanotubes on an ITO substrate. Figure 5 shows top- and side-view SEM images of a V_2O_5 nanotube array grown within the pores of a PC membrane after the membrane was dissolved away in methylene chloride. These nanotubes

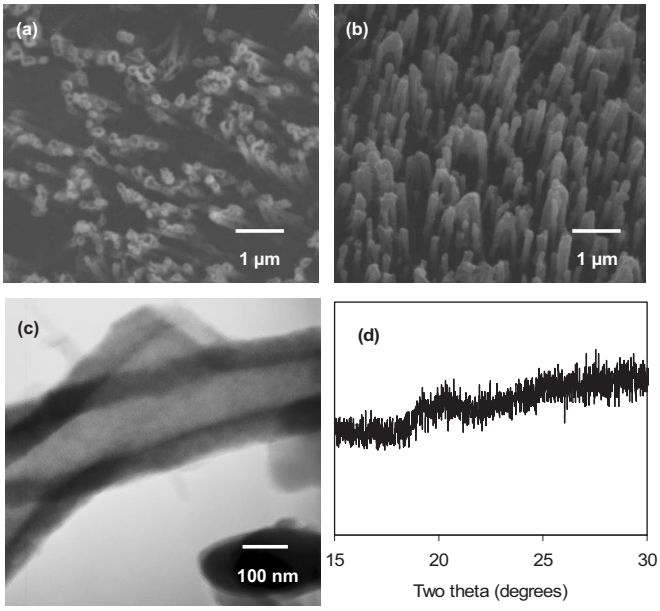

Figure 5. a) Top- and b) side-view SEM images of V_2O_5 nanotubes electrochemically deposited within 200 nm diameter pores of a PC membrane after the membrane was dissolved away in methylene chloride. c) TEM image of isolated V_2O_5 nanotubes. d) XRD pattern of the electrochemically prepared V_2O_5 film on a Au electrode. Reproduced with permission from [48]; copyright 2005, American Chemical Society.

stand apart from each other and project straight up from the substrate surface, and have a length of 10 µm (not shown). As can be seen from the TEM image in Figure 5c, the outer diameter of the nanotube is about 200 nm, while the inner diameter is about 100 nm. No electron diffraction pattern in TEM was observed, which suggests the amorphous nature of these nanotubes. XRD analysis of the nanotube arrays also shows their amorphous state. A possible mechanism of the nanotube growth is proposed as follows: A very thin coating of Au–Pd alloy on the PC membrane results in coating of the metal onto the edges of pores, leading to a high current density on these edges, where electrochemical reaction and deposition are initiated. On the edges of pores, the ionic cluster VO^{2+} is oxidized, depositing V_2O_5 through the following reaction:

$$2\,VO^{2+} + 3\,H_2O \rightarrow V_2O_5 + 6\,H^+ + 2\,e^- \quad (2)$$

Simultaneously a reduction reaction occurs at the counter electrode:

$$2\,H^+ + 2\,e^- \rightarrow H_2(g) \quad (3)$$

ADVANCED FUNCTIONAL MATERIALS

Figure 6a shows the first three voltammetric cycles of the $V_2O_5{\cdot}n\,H_2O$ nanotube arrays in the potential range between –1.6 and 0.4 V versus Ag/Ag^+, which were obtained using a scan rate of 10 mV s^{-1}. The CV of the nanotube arrays shows cathodic peaks at –0.3 and –1.2 V, corresponding to Li^+ intercalation; and anodic oxidation peaks at 0.17 and 0.4 V, which are attributed to Li^+ extraction. It can be seen from Figure 6a that these cathodic and anodic peaks flatten and the areas of the voltammograms shrink under the electrochemical redox cycles, indicating that the material loses some electroactivity. The degradation may be either ascribed to the electrochemically deposited $V_2O_5{\cdot}n\,H_2O$ itself or to the fragile structure of the nanotubes. Consistent with the cyclic voltammograms, chronopotentiograms have also shown that nanotube arrays exhibit degradation in electrochemical performance and the quantitative results of capacities calculated from chronopotentiometric measurements are discussed as follows. Figure 6b illustrates the dependence of discharge capacity on cycle number for both the nanotube array and film prepared from the electrochemical-deposition method. The capacity of the nanotube array is calculated based on an outer diameter of 200 nm, an inner diameter of 100 nm, a length of 10 μm, and a density of 2.87 g cm^{-3}.[65] The $V_2O_5{\cdot}n\,H_2O$ nanotube arrays demonstrate an initial high capacity of 300 mA h g^{-1}, about twice the initial capacity of 140 mA h g^{-1} obtained from the $V_2O_5{\cdot}n\,H_2O$ film. Such enhancement of capacity is due to the large surface area and short diffusion distances offered by the nanotube array. However, the capacity of the nanotube array decreased to 200 mA h g^{-1} in the second cycle and 180 mA h g^{-1} in the third. The degradation is slower in further cycles and the capacity finally stabilizes at 160 mA h g^{-1} after the sixth cycle, which is about 30 % higher than the stabilized capacity of the $V_2O_5{\cdot}n\,H_2O$ film. Our further work on the electrochemical intercalation properties of V_2O_5 films up to 50 cycles revealed little or no further degradation after the initial five to ten cycles.[59] The initial degradation of the $V_2O_5{\cdot}n\,H_2O$ film suggests that $V_2O_5{\cdot}n\,H_2O$ itself prepared from electrochemical deposition has some drawback and suffers a slight loss in electroactivity during cycling. However, the nanotube array shows a more drastic decay of initial performance compared to the film during cycling, possibly due to the morphological flexibility and fragility of the nanotubes, which has also been speculated in the literature.[33]

2.3. Ni/$V_2O_5{\cdot}n\,H_2O$ Core/Shell Nanocable Arrays

A two-step electrodeposition method has been used to prepare Ni/$V_2O_5{\cdot}n\,H_2O$ core/shell nanocable arrays.[49] Ni nanorod arrays were first grown by template-based electrochemical deposition. In the second step, a hydrated vanadium pentoxide shell was deposited onto the surface of nickel nanorods by sol electrophoretic deposition. Ni nanorod arrays were grown from a commercial Ni plating solution (NKBP11; Caswell, Newark, NY) inside PC templates by electrochemical deposition. The distance between the two electrodes was kept at 25 mm. The applied voltage was 2.0 V, and the deposition lasted up to 3 h. Upon completion of the deposition, the samples were dried at 110 °C for 12 h in air. Dried samples were subsequently attached to a titanium plate using silver paste. The samples on the titanium plates were then immersed in ethylene chloride to dissolve the PC membrane, resulting in the formation of freestanding Ni nanorod arrays attached to a titanium plate. In the second step, the Ni nanorod arrays were coated with a thin layer of $V_2O_5{\cdot}n\,H_2O$ by sol electrophoretic deposition. From this sol, a thin layer of $V_2O_5{\cdot}n\,H_2O$ was coated onto the Ni nanorods using electrophoretic deposition. The applied voltage was 0.8 V and the deposition lasted up to 15 min.

Figure 7 shows typical SEM images of a Ni nanorod array, grown in a 200 nm PC membrane under an applied voltage of 2.0 V, after the PC membrane was dissolved in ethylene chloride and a Ni/$V_2O_5{\cdot}n\,H_2O$ core/shell nanocable array, with the $V_2O_5{\cdot}n\,H_2O$ layer deposited under an applied voltage of –0.8 V. The Ni nanorod arrays grown by electrochemical deposition have a diameter of ca. 200 nm and grow perpendicular

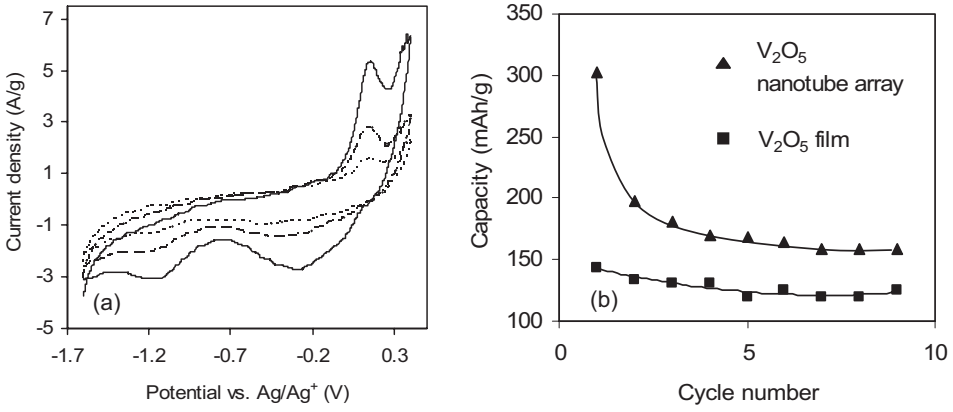

Figure 6. a) CVs of the V_2O_5 nanotube array in the potential range from –1.6 to 0.4 V versus Ag/Ag^+, obtained using a scan rate of 10 mV s^{-1}; solid line: the first cycle; dashed line: the second cycle; dotted line: the third cycle. b) Dependence of the discharge capacity on the cycle number obtained from chronopotentiometric measurements at a cutoff voltage of 0.4 to –1.5 V versus Ag/Ag^+. Reproduced with permission from [48]; copyright 2005, American Chemical Society.

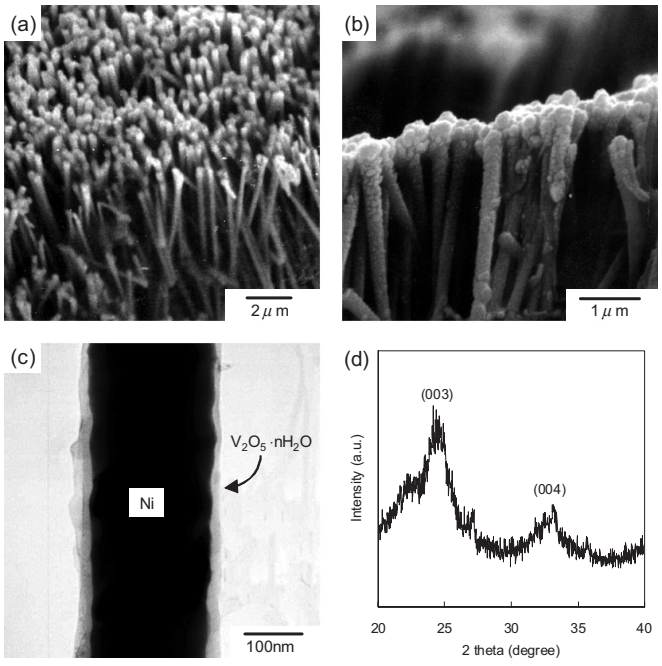

Figure 7. SEM image of a) a Ni nanorod array grown in a 200 nm PC membrane under an applied voltage of 2.0 V after dissolving the PC membrane in ethylene chloride, and b) V_2O_5-coated Ni nanorods under an applied voltage of –0.8 V. c) TEM image of a Ni/V_2O_5 core/shell nanocable. d) XRD pattern of a V_2O_5 film grown by sol electrophoretic deposition. Reproduced with permission from [49]; copyright 2005, American Chemical Society.

to the substrate. Figure 7c shows a TEM image of a Ni/$V_2O_5 \cdot n\,H_2O$ core/shell nanocable. The image of the nanocable shows a dark central area surrounded by a lighter area along the axis. This morphology clearly suggests that the nanocable has a layered structure with different composition in the radial direction; the dark area is likely to be Ni and the outer area, $V_2O_5 \cdot n\,H_2O$. The core material is covered completely and uniformly by a $V_2O_5 \cdot n\,H_2O$ shell with a thickness ranging from 30 to 50 nm based on SEM and TEM results. It should be noted that the interface between Ni and $V_2O_5 \cdot n\,H_2O$ is not microscopically smooth, which may be attributable to the nature of the Ni nanorod formed by electrochemical deposition. XRD analyses of the nanocable arrays revealed the presence of only Ni. The $V_2O_5 \cdot n\,H_2O$ coating is too thin to be detected, although energy dispersive X-ray spectroscopy unambiguously revealed the presence of vanadium and oxygen. Figure 7d shows the XRD pattern of the $V_2O_5 \cdot n\,H_2O$ film grown by electrophoretic deposition from the same sol and identical voltage, suggesting the coating layer is $V_2O_5 \cdot n\,H_2O$.

Figure 8a compares the CVs of Ni/$V_2O_5 \cdot n\,H_2O$ nanocable arrays and arrays of single-crystal V_2O_5 nanorods; these results unambiguously demonstrate the better electrochemical properties of Ni/$V_2O_5 \cdot n\,H_2O$ nanocable arrays compared to the arrays of single-crystal V_2O_5 nanorods. Figure 8b summarizes the Li^+-intercalation capacity as a function of current density for Ni/$V_2O_5 \cdot n\,H_2O$ nanocable arrays, single-crystal V_2O_5 nanorod arrays, and V_2O_5 films. The intercalation capacities of both nanorod arrays and sol–gel films decrease rapidly as the current density increases, while the nanocable arrays are able to retain the high intercalation capacity at high current density (discharge rate), indicating the excellent high-rate performance of nanocable arrays. Figure 8c shows that Ni/$V_2O_5 \cdot n\,H_2O$ nanocable array has significantly enhanced energy density and power density than the nanorod array and sol–gel film by at least one order of magnitude.

2.4. Nanostructured V_2O_5 Films with Various Features

Platelet- and fibrillar-structured V_2O_5 films have been prepared by solution methods and the discharge capacities and cyclic performance of these films were compared with the conventional plain structured film.[57] The platelet film consists of 20–30 nm sized V_2O_5 particles with random orientation, whereas the fibrillar film is comprised of randomly oriented fibers with most of them protruding from the substrate surface. The initial discharge capacities of platelet- and fibrillar-structured V_2O_5 films are 1240 and 720 mA h g^{-1}, respectively, which are far larger than the initial discharge value (260 mA h g^{-1}) of the plain film. Such large discharge-capacity values are ascribed to the combined effects of reduced Li^+-diffusion distance, which prevents concentration polarization of Li^+ in the V_2O_5 electrode, and poor interlayer crosslinking, which offers more Li^+ intercalation. However, platelet- and fibrillar-structured V_2O_5 films were easily degraded during

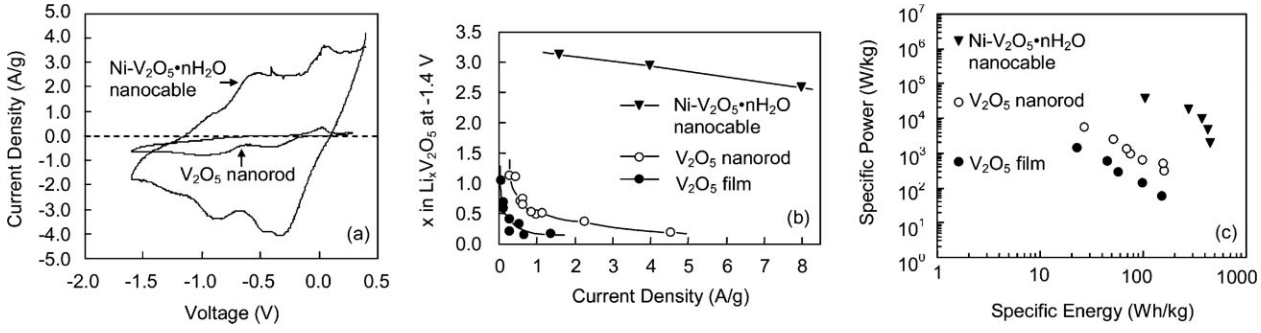

Figure 8. a) CVs obtained using a scan rate of 10 mV s^{-1}. b) Relationship between current density and amount of Li intercalated per mole of V_2O_5 calculated from chronopotentiometric measurements. c) Ragone plot for the Ni/$V_2O_5 \cdot n\,H_2O$ nanocable array, and the V_2O_5 nanorod array and film. Reproduced with permission from [49]; copyright 2005, American Chemical Society.

ADVANCED FUNCTIONAL MATERIALS

electrochemical cyclic tests. Figure 9 shows SEM images of the surface morphology of the resulting films. The V_2O_5 film made from the V_2O_5 sol (see Fig. 1a) shows a typical smooth surface with some voids throughout the film. The film prepared using $VOSO_4$ shows a randomly oriented platelet-like morphology with most platelets standing almost vertically and usually having a thickness of 20–30 nm, as shown in Figure 9b. Figure 9c shows the film prepared using the VO^{2+} solution; the film shows an assembly of fibrillar particles 20–40 nm in diameter protruding from the current-collector surface like the bristles of a brush.

3. Engineering of Crystallinity and Interlayer Structure of Vanadium Oxide

In addition to making use of nanostructures, another approach to improve the Li^+-intercalation performance in vanadium pentoxide is to modify its crystallinity or interlayer spacing. Most recently, Lee and Cao have found that the electrochemical intercalation properties of V_2O_5 have been significantly enhanced with the addition of TiO_2.[59] It is also well known that the presence of TiO_2 appreciably improves the cyclic-fatigue resistance of V_2O_5.[59] $V_2O_5{\cdot}n\,H_2O$ has a higher intercalation capacity than orthorhombic V_2O_5, however, $V_2O_5{\cdot}n\,H_2O$ may suffer from poor cycling life, possibly due to the reaction between lithium and the water in $V_2O_5{\cdot}n\,H_2O$ to form Li_2O.[66,67] It has been found that $V_2O_5{\cdot}n\,H_2O$ exhibits a large capacity and good cycling performance when the water content in $V_2O_5{\cdot}n\,H_2O$ is reduced by thermal treatment; the influence of heat treatment on $V_2O_5{\cdot}n\,H_2O$ has been studied using $V_2O_5{\cdot}n\,H_2O$ synthesized from the $NaVO_3$ route[39,68–70] and, more recently, on that synthesized by the H_2O_2–V_2O_5 route.[58]

3.1. Enhancement of Intercalation Properties of V_2O_5 Films and Nanorod Arrays by TiO_2 Addition

Although it is well documented that TiO_2 incorporation can greatly improve the cyclic stability of V_2O_5, the influence of TiO_2 addition on the Li^+-intercalation properties of V_2O_5 remains an issue of debate. The roots of this disagreement may lie in the fact that the electrochemical performance of the electrode is strongly dependent on its fabrication method, morphology, and crystallinity. Lee and Cao have presented a systematic investigation of the preparation and intercalation properties of V_2O_5/TiO_2 mixture films, which demonstrates that high Li^+-intercalation rates and capacity in V_2O_5 films are achievable with TiO_2 addition. For example, the addition of 20 mol % Ti into polycrystalline V_2O_5 demonstrated an approximately 100 % improvement in Li^+-intercalation performance over single V_2O_5 electrodes. Such an enhancement in the intercalation properties of V_2O_5 films with TiO_2 addition was attributed to changes in microstructure, crystallinity, and also a possible lattice structure and interaction force between adjacent layers in V_2O_5. Following this report on V_2O_5/TiO_2 films, we have prepared V_2O_5/TiO_2 composite nanorod arrays with various V/Ti ratios, and have investigated their intercalation properties systematically.[60]

V_2O_5/TiO_2 composite nanorod arrays were grown in PC templates by means of capillary-force-induced filling. The templates used were radiation-track-etched hydrophilic PC membranes with pore diameters of 400 nm and a thickness of 10 μm. The precursor solutions were made of mixtures of $VOSO_4$ and $TiOSO_4$. The $VOSO_4$ specifications were mentioned in the section on processing methods above. The $TiSO_4$ solution was prepared by diluting $TiOSO_4$ solution (15 wt % in diluted H_2SO_4, Aldrich) with deionized H_2O to a concentration of 0.1 M; its pH value was adjusted to 1.8 by adding $NH_3{\cdot}H_2O$. VO^{2+} and TiO^{2+} solutions were then aged for a week in air and admixed in molar ratios of 75:25 and 50:50. An excessive amount of the precursor solution was dropped onto ITO substrates and a PC membrane was placed on top of the solution at ambient pressure and room temperature for 4 h to allow complete filling and solidification of solution. The filled template on the ITO substrate was then dried at 70 °C for 8 h in air and fired at 485 °C for 1 h to remove the PC membranes through pyrolysis and oxidation, as well as to densify the nanorod arrays. Pure V_2O_5 nanorod arrays were obtained by filling the $V_2O_5{\cdot}n\,H_2O$ sol into the 400 nm diameter pores of the PC membranes through a similar process. The filled template on the ITO substrate was dried at 110 °C for 8 h in air before staying under ambient conditions for 4 h. The sample was then heated at 485 °C for 1 h to remove the PC membranes. Figure 10 shows typical SEM images of pure V_2O_5 nanorod arrays

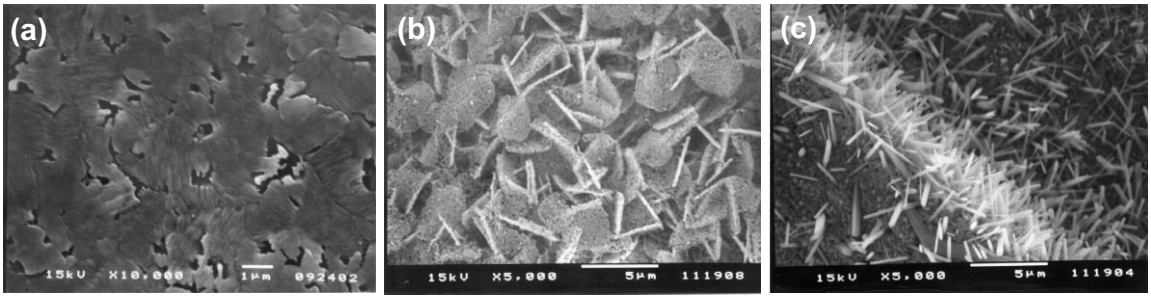

Figure 9. SEM images of as-prepared V_2O_5 thin films: a) plain film, b) in situ grown platelet-structured film, and c) in situ grown fibrillar-structured film. Reproduced with permission from [57]; copyright 2005, American Chemical Society.

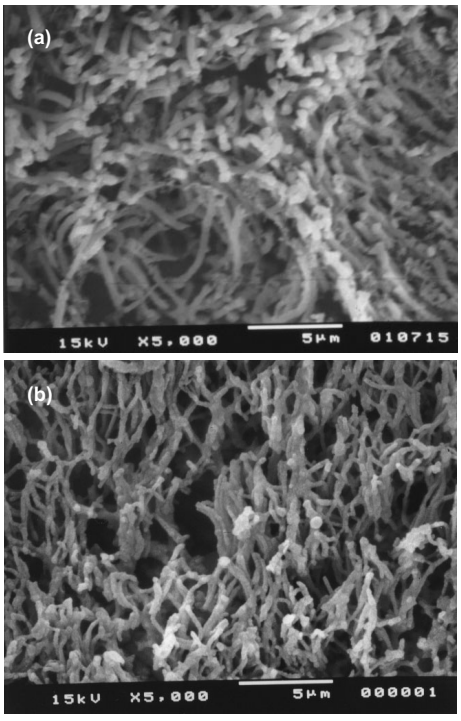

Figure 10. SEM images of a) pure V_2O_5 nanorods grown in PC membranes with 400 nm diameter pores using the capillary-force method and heated at 485 °C, and b) V_2O_5/TiO_2 (molar ratio V/Ti=50:50) composite nanorod arrays. Reproduced with permission from [60]; copyright 2005, SpringerLink.

and V_2O_5/TiO_2 composite nanorods (molar ratio V/Ti=50:50) grown in 400 nm PC membranes and heated at 485 °C for 1 h in air. These nanorods project from the surface of the ITO substrate like bristles of a brush, and the V_2O_5/TiO_2 composite nanorods are less smooth than the pure V_2O_5 nanorods. V_2O_5/TiO_2 nanorods (molar ratio V/Ti=75:25) have a similar morphology to composite nanorods with a molar ratio of V/Ti = 50:50, therefore their SEM image is not shown here.

XRD patterns of the V_2O_5/TiO_2 nanorod arrays show that the crystalline V_2O_5 phase and the TiO_2 anatase phase coexist.[60] In this research, $VOSO_4$ (valence state of V is +4) was used as the precursor material for preparing the V_2O_5/TiO_2 composite nanorod array. Although VO_2 can form a solid solution with TiO_2, XRD patterns indicate that no solid solutions were formed in this study. The nanorods studied are basically a mixture of vanadium pentoxide and anatase phase, suggesting V(+4) has been oxidized to V(+5) during the processing. Careful comparison of XRD patterns suggests that the crystallinity of both TiO_2 and V_2O_5 phases deteriorated when the other phase was present. The hindrance of crystallization in mixed-oxide systems is a known phenomenon caused by the increased diffusion requirement for the crystallization processes to occur in the mixed system. In our separate study, it was found that the presence of other phases indeed resulted in an appreciable reduction in grain size and a change in morphology of both the V_2O_5 and TiO_2 phases.[59]

Figure 11a summarizes and compares the Li^+-intercalation capacity as a function of current density for nanorod arrays with three V/Ti molar ratios. The Li^+-intercalation capacity of the V_2O_5/TiO_2 (V/Ti = 75:25, molar ratio) nanorod array is the highest, followed by that of the pure V_2O_5 nanorod array, and then the V_2O_5/TiO_2 (V/Ti = 50:50, molar ratio) array. Figure 11b illustrates the changes in discharge capacity with molar fraction V/(V+Ti) at a given current density. It is clear that nanorod arrays with a V/Ti molar ratio of 75:25 have the highest energy-storage capacity at all current densities. Such a result is similar to that found in Lee and Cao's work on V_2O_5/TiO_2 composite films.[59]

3.2. Enhancement of Intercalation Properties of $V_2O_5 \cdot n\,H_2O$ Films by Controlling Water Content

Films of $V_2O_5 \cdot n\,H_2O$ were prepared by coating a $V_2O_5 \cdot n\,H_2O$ sol onto ITO substrates. The samples were then dried under ambient conditions and annealed at various temperatures (110, 250, 300, and 330 °C) in air for 5 h. All the films were coherent and homogenous. In general, $V_2O_5 \cdot n\,H_2O$ films have a smooth and featureless surface morphology; no detectable cracks or pinholes were observed and the thickness of the films was ca. 1 μm. There was no appreciable difference in surface morphology or thickness for films obtained at room temperature or annealed at a temperature ≤ 250 °C.

The thermogravimetric traces for $V_2O_5 \cdot n\,H_2O$ xerogels reveal the existence of 1.6 moles of water per mole of oxide at room temperature (assuming V_2O_5 as the solid phase after heating at >330 °C, whereas water is the only volatile phase in the initial film). This result and the shape of the thermogravimetric analysis (TGA) curve are similar to those obtained for xerogels prepared by the $NaVO_3$ and alkoxide routes.[71] The weight-change profile for the xerogel is characterized by a steep loss between room temperature and 100 °C, followed by a more gradual weight loss up until 330 °C. Thermal treatment at 110 °C produced a xerogel with the $V_2O_5 \cdot 0.6\,H_2O$ composi-

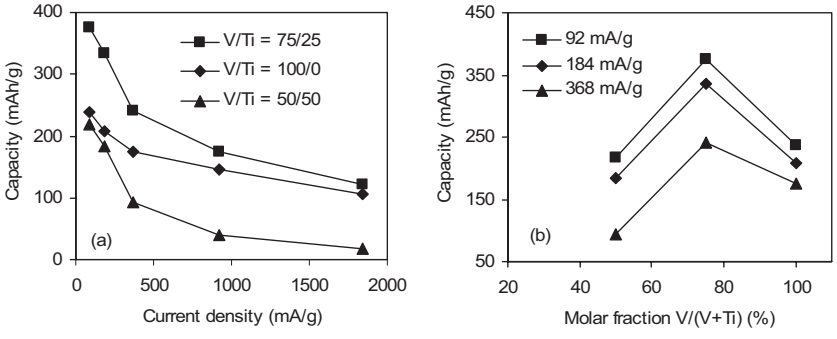

Figure 11. a) Li^+-intercalation capacity versus current density for V_2O_5/TiO_2 nanorods with various V/Ti molar ratios, and b) Li^+-intercalation capacity versus molar fraction of vanadium at various current densities. Reproduced with permission from [60]; copyright 2005, SpringerLink.

ADVANCED FUNCTIONAL MATERIALS

tion. Continued heating to 250 °C produced $V_2O_5{\cdot}0.3\,H_2O$ by removing bound water. Heating above 300 °C induced loss of tightly bound water and material crystallization, as discussed in the XRD results.

For $V_2O_5{\cdot}n\,H_2O$, the interlayer spacing can be calculated from the diffraction angle of the (001) peak.[72,73] Figure 12a summarizes the dependence of interlayer spacing on n in $V_2O_5{\cdot}n\,H_2O$. For samples treated at 25, 110, and 250 °C, the interlayer spacings show a slight decrease from 11.74 to 11.15 Å as the temperature increases; however, the change is rather small and the results are consistent with the 11.5 Å reported in previous reports.[22] For the sample annealed at 300 °C, in which low-crystalline $V_2O_5{\cdot}n\,H_2O$ coexists with orthorhombic V_2O_5, the interlayer spacing of $V_2O_5{\cdot}n\,H_2O$ is 8.43 Å, apparently smaller than the samples treated from 25 to 250 °C. TGA results have shown that 110 °C corresponds to $V_2O_5{\cdot}0.6\,H_2O$ and 250 °C to $V_2O_5{\cdot}0.3\,H_2O$. It can be concluded that the interlayer spacing does not change much when only bound water (reversibly absorbed or hydrogen-bonded water) is removed. These parameters will change considerably only when tightly bound (chemically bonded) water is removed and the material is on the verge of crystallization. Figure 12b summarizes and compares the cycling performance of the $V_2O_5{\cdot}n\,H_2O$ films treated at 25, 110, 250, and 300 °C at the high current density of 100 $\mu A\,cm^{-2}$. It can be seen that the capacities of all three films degrade initially then become more or less stabilized. The film obtained at 25 °C has the lowest capacity and the least-satisfying cycling performance among the three xerogel films. The film annealed at 300 °C has a high initial capacity; however, it shows the most drastic electrochemical degradation, possibly due to the crystalline phase. The film annealed at 250 °C delivers the highest initial capacity and retains a stable capacity of 185 $mA\,h\,g^{-1}$ after 20 cycles. The reason is explained as follows: Removing too little water limits the electrochemical performance because a significant amount of water may react with lithium to form Li_2O. Removal of too much water also deteriorates the intercalation performance, because of the shrinkage of the interlayer distance and the emergence of the crystallization phase. $V_2O_5{\cdot}0.3\,H_2O$ obtained at 250 °C was found to be an optimal composition, which has least possible amount of water and keeps the large interlayer distance and the amorphous phase.

4. Concluding Remarks

We have presented a review on improving Li^+-intercalation properties in vanadium pentoxides by engineering their nanostructure and interlayer structure. First, the template-based method was utilized to prepare various nanostructures, such as single-crystal V_2O_5 nanorod arrays, $V_2O_5{\cdot}n\,H_2O$ nanotube arrays, and $Ni/V_2O_5{\cdot}n\,H_2O$ core/shell nanocable arrays. All the resultant nanoarrays consist of uniformly sized, 10 μm long nanorods/nanotubes/nanocables of vanadium pentoxide projecting from the substrate surface. The morphology, structure, and the growth mechanism of these nanostructures have been discussed. The Li^+-intercalation properties of the nanostructured electrodes have been investigated and compared to those of the vanadium pentoxide film electrode. Electrochemical analysis has demonstrated that all the nanostructured electrodes exhibit significantly improved storage capacity and rate performance over those of V_2O_5 films, because of the larger surface areas and the shorter diffusion paths. In particular, the $Ni/V_2O_5{\cdot}n\,H_2O$ core/shell nanocable demonstrates the best electrochemical performance among the three. The second part of this work investigated the effect of modifying the interlayer structure on the Li^+-intercalation properties in vanadium pentoxides. Specifically, for the orthorhombic V_2O_5 phase, a capillary-enforced template-based method has been applied to fabricate the V_2O_5/TiO_2 composite nanorod arrays by filling a mixture of $VOSO_4$ and $TiOSO_4$ solutions into the pores of a PC membrane. Addition of TiO_2 to orthorhombic V_2O_5 has been found to improve the Li^+-intercalation performance of V_2O_5. Such enhancement is ascribed to changes in crystallinity and possible lattice structure and interaction force between adjacent layers in V_2O_5. Further, the Li^+-intercalation properties of low-crystalline $V_2O_5{\cdot}n\,H_2O$ can be improved by controlling the water content through thermal annealing. Electrochemical characterizations have demonstrated that the $V_2O_5{\cdot}0.3\,H_2O$ film exhibits a higher Li^+-intercalation capacity and more sustainable cycling life than the anhydrous crystalline V_2O_5 film or other $V_2O_5{\cdot}n\,H_2O$ films (n =0.1, 0.6, 1.6). The enhanced electrochemical property is attributed to the reduced water content, the retained interlayer spacing, and the dominant amorphous phase. The processing methods mentioned in this article are generally applicable to fabricating nanostructures of other oxides, e.g., metal oxide core/shell nanocable arrays. Discussion of the underlying principle that affects the Li^+-intercalation properties of V_2O_5 in the present work can be helpful to the further understanding of vanadium pentoxide and other intercalation materials.

Received: September 12, 2005
Final version: November 9, 2005
Published online: April 24, 2006

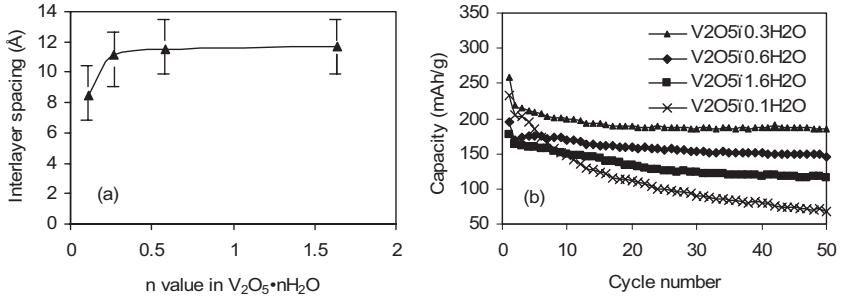

Figure 12. a) Dependence of interlayer spacing on the n value in $V_2O_5{\cdot}n\,H_2O$. b) Cycling performance at a current density of 100 $\mu A\,cm^{-2}$ for $V_2O_5{\cdot}n\,H_2O$ films of various n values. The voltage ranges from 0.4 to –1.6 V vs. Ag/Ag^+. Reproduced with permission from [58]; copyright 2005, American Chemical Society.

[1] J. N. Reimers, J. R. Dahn, *J. Electrochem. Soc.* **1992**, *139*, 2091.
[2] P. N. Kumta, D. Gallet, A. Waghray, G. E. Blomgren, M. P. Setter, *J. Power Sources* **1998**, *72*, 91.

[3] T. Ohzuku, A. Ueda, N. Nagayama, Y. Iwakoshi, H. Komori, *Electrochim. Acta* **1993**, *38*, 1159.
[4] G. G. Amatucci, J. M. Tarascon, L. C. Klein, *J. Electrochem. Soc.* **1996**, *143*, 1114.
[5] T. Ohzuku, A. Ueda, *Solid State Ionics* **1994**, *69*, 201.
[6] T. Ohzuku, A. Ueda, N. Nagayama, *J. Electrochem. Soc.* **1993**, *140*, 1862.
[7] J. R. Dahn, U. von Sacken, C. A. Michal, *Solid State Ionics* **1990**, *44*, 87.
[8] A. Rougier, P. Gravereau, C. Delmas, *J. Electrochem. Soc.* **1996**, *143*, 1168.
[9] L. Abello, E. Husson, Y. R. Repelin, G. Lucazeau, *Spectrochim. Acta Part A* **1983**, *39*, 641.
[10] M. M. Thackeray, *J. Electrochem. Soc.* **1995**, *142*, 2558.
[11] M. Winter, J. O. Besenhard, M. E. Spahr, P. Novák, *Adv. Mater.* **1998**, *10*, 725.
[12] C. R. Sides, N. Li, C. J. Patrissi, B. Scrosati, C. R. Martin, *MRS Bull.* **2002**, *27*, 604.
[13] A. Aricò, P. Bruce, B. Scrosati, J. Tarascon, W. Schalkwijk, *Nat. Mater.* **2005**, *4*, 366.
[14] J. P. Maranchi, O. I. Velikokhatny, M. K. Datta, I. S. Kim, P. N. Kumta, in *Chemical Processing of Ceramics* (Eds: B. Lee, S. Komarneni), Marcel Dekker, New York **2005**, p. 667.
[15] D. W. Murphy, P. A. Christian, F. J. DiSalvo, J. V. Waszczak, *Inorg. Chem.* **1979**, *18*, 2800.
[16] D. W. Murphy, in *Intercalation Chemistry* (Eds: M. S. Whittingham, A. J. Jacobsen), Academic Press, New York **1982**, p. 563.
[17] *Inorganic Crystal Structures* (Eds: B. G. Hyde, S. Anderson), Wiley, New York **1989**, p. 16.
[18] Y. Sakurai, S. Okada, J. Yamaki, T. Okada, *J. Power Sources* **1987**, *20*, 173.
[19] K. West, B. Zachau-Christiansen, M. J. L. Ostergard, T. Jacobsen, *J. Power Sources* **1987**, *20*, 165.
[20] K. West, B. Zachau-Christiansen, T. Jacobsen, S. Skaarup, *Electrochim. Acta* **1993**, *38*, 1215.
[21] K. Salloux, F. Chaput, H. P. Wong, B. Dunn, M. W. Breiter, *J. Electrochem. Soc.* **1995**, *142*, L191.
[22] V. Petkov, P. N. Trikalitis, E. S. Bozin, S. J. L. Billinge, T. Vogt, M. G. Kanatzidis, *J. Am. Chem. Soc.* **2002**, *124*, 10 157.
[23] F. Coustier, J. Hill, B. B. Owens, S. Passerini, W. H. Smyrl, *J. Electrochem. Soc.* **1999**, *146*, 1355.
[24] J. Livage, *Chem. Mater.* **1991**, *3*, 578.
[25] E. Portiron, A. L. Salle, A. Varbaere, Y. Piffard, D. Guyomard, *Electrochim. Acta* **1999**, *44*, 197.
[26] F. Lantelme, A. Mantoux, H. Groult, D. Lincot, *J. Electrochem. Soc.* **2003**, *150*, A1202.
[27] M. Hibino, M. Ugaji, A. Kishimoto, T. Kudo, *Solid State Ionics* **1995**, *79*, 239.
[28] Y. Wang, K. Lee, H. Shang, B. Wiley, Y. Xia, G. Z. Cao, *Phys. Status Solidi A* **2005**, *202*, R79.
[29] C. J. Patrissi, C. R. Martin, *J. Electrochem. Soc.* **1999**, *146*, 3176.
[30] M. E. Spahr, P. Bitterli, R. Nesper, M. Müller, F. Krumeich, H. U. Nissen, *Angew. Chem. Int. Ed.* **1998**, *37*, 1263.
[31] M. E. Spahr, P. Stoschitzki-Bitterli, R. Nesper, O. Haas, P. Novák, *J. Electrochem. Soc.* **1999**, *146*, 2780.
[32] A. Dobley, K. Ngalas, S. Yang, P. Y. Zavalij, M. S. Whittingham, *Chem. Mater.* **2001**, *13*, 4382.
[33] G. R. Patzke, F. Krumeich, R. Nesper, *Angew. Chem. Int. Ed.* **2002**, *41*, 2446.
[34] K. Takahashi, S. J. Limmer, Y. Wang, G. Z. Cao, *J. Phys. Chem. B* **2004**, *108*, 9795.
[35] V. Petkov, P. N. Trikalitis, E. S. Bozin, S. J. L. Billinge, T. Vogt, M. G. Kanatzidis, *J. Am. Chem. Soc.* **2002**, *124*, 10 157.
[36] J. Wang, C. J. Curtis, D. L. Schulz, J. Zhang, *J. Electrochem. Soc.* **2004**, *151*, A1.
[37] K. West, B. Zachau-Christinansen, T. Jacobeen, *J. Power Sources* **1993**, *43–44*, 127.
[38] A. K. Cuentas-Gallegos, P. Gómez-Romero, in *New Trends in Intercalation Compounds for Energy Storage* (Eds: C. Julien, J. P. Pereira-Ramos, A. Momchilov), Kluwer Academic Publisher, Dordrecht, The Netherlands **2002**, p. 535.
[39] C. A. Brunello, C. F. O. Graeff, *J. Non-Cryst. Solids* **2002**, *304*, 265.
[40] F. Artuso, F. Bonino, F. Decker, A. Lourenco, E. Masetti, *Electrochim. Acta* **2002**, *47*, 2231.
[41] F. Varsano, F. Decker, E. Masetti, F. Croce, *Electrochim. Acta* **2001**, *46*, 2069.
[42] B. B. Owens, S. Passerini, W. H. Smyrl, *Electrochim. Acta* **1999**, *44*, 215.
[43] M. G. Minett, J. R. Owen, *J. Power Sources* **1990**, *32*, 81.
[44] A. Davies, R. J. Hobson, M. J. Hudson, W. J. Macklin, R. J. Neat, *J. Mater. Chem.* **1996**, *6*, 49.
[45] N. Özer, S. Sabuncu, J. Cronin, *Thin Solid Films* **1999**, *338*, 201.
[46] K. Takahashi, S. J. Limmer, Y. Wang, G. Z. Cao, *Jpn. J. Appl. Phys., Part 1* **2005**, *44*, 662.
[47] K. Takahashi, Y. Wang, G. Z. Cao, *Appl. Phys. Lett.* **2005**, *86*, 053 102.
[48] Y. Wang, K. Takahashi, H. Shang, G. Z. Cao, *J. Phys. Chem. B* **2005**, *109*, 3085.
[49] K. Takahashi, Y. Wang, G. Z. Cao, *J. Phys. Chem. B* **2005**, *109*, 48.
[50] S. J. Limmer, S. Seraji, M. J. Forbess, Y. Wu, T. P. Chou, C. Nguyen, G. Z. Cao, *Adv. Mater.* **2001**, *13*, 1269.
[51] S. J. Limmer, S. Seraji, M. J. Forbess, Y. Wu, T. P. Chou, C. Nguyen, G. Z. Cao, *Adv. Funct. Mater.* **2002**, *12*, 59.
[52] S. J. Limmer, G. Z. Cao, *Adv. Mater.* **2003**, *15*, 427.
[53] S. J. Limmer, T. P. Chou, G. Z. Cao, *J. Mater. Sci.* **2004**, *39*, 895.
[54] S. J. Limmer, S. Vince Cruz, G. Z. Cao, *Appl. Phys. A* **2004**, *79*, 421.
[55] S. J. Limmer, T. L. Hubler, G. Z. Cao, *J. Sol-Gel Sci. Technol.* **2003**, *26*, 577.
[56] G. Z. Cao, *J. Phys. Chem. B* **2004**, *108*, 19 921.
[57] K. Lee, Y. Wang, G. Z. Cao, *J. Phys. Chem. B* **2005**, *109*, 16 700.
[58] Y. Wang, H. Shang, T. Chou, G. Z. Cao, *J. Phys. Chem. B* **2005**, *109*, 11 361.
[59] K. H. Lee, G. Z. Cao, *J. Phys. Chem. B* **2005**, *109*, 11 880.
[60] K. Takahashi, Y. Wang, K. H. Lee, G. Z. Cao, *Appl. Phys. A* **2006**, *82*, 27.
[61] A. van der Drift, *Philips Res. Rep.* **1968**, *22*, 267.
[62] R. L. Penn, J. F. Banfield, *Geochim. Cosmochim. Acta* **1999**, *63*, 1549.
[63] C. M. Chun, A. Navrotsky, I. A. Aksay, in *Proc. Microscopy and Microanalysis* (Ed: G. W. Bailey), Jones and Begell Publishing, New York **1995**, p. 188.
[64] R. D. Rauh, *Electrochim. Acta* **1999**, *44*, 3165.
[65] Y. J. Liu, J. A. Cowen, T. A. Kaplan, D. C. DeGroot, J. Schindler, C. R. Kannewurf, M. G. Kanatzidis, *Chem. Mater.* **1995**, *7*, 1616.
[66] D. Linden, in H*andbook of Batteries*, 2nd ed., McGraw-Hill, New York **1995**.
[67] E. C. Almeida, M. Abbate, J. M. Rosolen, *Solid State Ionics* **2001**, *140*, 241.
[68] J. Wang, C. J. Curtis, D. L. Schulz, J. Zhang, *J. Electrochem. Soc.* **2004**, *151*, A1.
[69] K. West, B. Zachau-Christinansen, T. Jacobeen, *J. Power Sources* **1993**, *43–44*, 127.
[70] C. A. Brunello, C. F. O. Graeff, *J. Non-Cryst. Solids* **2002**, *304*, 265.
[71] G. P. Hollad, F. Huguenin, R. M. Torresi, D. A. Buttry, *J. Electrochem. Soc.* **2003**, *150*, A721.
[72] G. Z. Cao, *Nanostructures and Nanomaterials: Synthesis, Properties and Applications*, Imperial College Press, London **2004**.
[73] L. S. Birks, H. Friedman, *J. Appl. Phys.* **1946**, *17*, 687.